Nanotechnology **21** (2010) 055707 (8pp) doi:10.1088/0957-4484/21/5/055707

Thermophysical properties of hydrogenated vanadium-doped magnesium porous nanostructures

Xiangwen Chen[1], Yuping He[2], Yiping Zhao[2] and Xinwei Wang[1,3]

[1] Department of Mechanical Engineering, 2010 H. M. Black Engineering Building, Iowa State University, Ames, IA 50011-2161, USA
[2] Department of Physics and Astronomy, and Nanoscale Science and Engineering Center, University of Georgia, Athens, GA 30602, USA

E-mail: xwang3@iastate.edu

Received 6 October 2009, in final form 25 November 2009
Published 24 December 2009
Online at stacks.iop.org/Nano/21/055707

Abstract
Vanadium-doped magnesium nanostructures are fabricated by an oblique angle co-deposition method and hydrogenated/dehydrogenated for 21 cycles. The effective thermal conductivity and density of the MgH_2 nanostructures is measured by using a photothermal system. A multilayer physical model is used to fit the experimental data. Our results show that the effective thermal conductivity of the hydrogenated V-doped Mg nanostructures is in the range of 1.16–2.40 W m^{-1} K^{-1} and the density falls in the range of 878–1320 kg m^{-3}. The measured density agrees well with the estimation from electron micrograph observation. Variation in the measurements indicates strong nonuniformity of the sample structure and thickness. Based on the measured density and effective thermal conductivity, the thermal conductivity of bulk V-doped Mg hydrides is also evaluated using Maxwell's correlation.

(Some figures in this article are in colour only in the electronic version)

1. Introduction

Hydrogen is a promising alternative energy source for fossil fuel. The practical use of hydrogen depends largely on on-board storage techniques [1]. Storing hydrogen as compressed gas in pressurized vessels or in the form of liquid in cryogenic tanks is the usual approach, and it requires high energy consumption and needs high-level safety precautions [1, 2]. Storing H_2 in solid state materials is the safest and most promising method [3]. In the pursuit of metal hydrides as solid state hydrogen storage media, magnesium hydride (MgH_2) is considered a good candidate due to its light weight, low manufacturing cost and high theoretical hydrogen storage capacity (∼7.66% by weight, and ∼150 kg H_2 m^{-3} by volume) [4, 5]. However, since the enthalpy of MgH_2 formation is very high (−76 kJ/mol H_2), it requires temperatures in excess of 573 K to decompose it into H_2 and bulk Mg [6]. Additionally, the kinetics of MgH_2 formation are slow [7, 8]. To solve these two problems, it has been reported that doping Mg with a transition metal (catalyst) can weaken the Mg–H bond and reduce the stability of the hydride, thus promoting the hydrogenation/dehydrogenation performance of Mg [6, 9–13]. Ball-milling is one of the primary methods to fabricate catalyst-doped Mg structures. The hydrogen storage properties of ball-milled nanocrystalline MgH_2 + 5 at.% Tm (Tm = Ti, V, Mn, Fe and Ni) were evaluated by Liang *et al* [14]. Their results revealed that the composite containing Ti or V exhibited the most rapid desorption kinetics at a temperature above 523 K and rapid absorption kinetics at temperatures as low as 302 K. Schulz *et al* [15] reported that V and Ti were better catalysts than Ni for hydrogen absorption and desorption in transition-metal-doped MgH_2. Pozzo and Alfe [6] investigated a wide range of transition metal dopants including Ti, Zr, V, Fe, Ru, Co, Rh, Ni, Pd, Cu and Ag. Their results showed that Ti, V and Zr, together with Ru, could eliminate the Mg–H dissociation barrier. Bobet *et al* used chemical fluid deposition in supercritical fluids (SCF) to fabricate doped metal hydrides [16]. Besides keeping the same sorption

[3] Author to whom any correspondence should be addressed.

properties as those fabricated by the ball-milling method, the materials fabricated by SCF had significantly improved cyclability. For ball-milling samples, the catalytic effect of metal decreased after 100 hydrogenation/dehydrogenation cycles, while for the SCF sample it almost stayed constant [16]. Other fabrication methods for doped metal hydrides, including chemical fluid deposition in supercritical fluids (SCF) [16], sol–gel [17], ion implantation [18], ultrasound radiation [19], electrodeposition [20], chemical vapor deposition [21] and hybrid growth techniques [22], have also been reported. Recently, we have successfully applied an oblique angle co-deposition technique (OACD) to fabricate Ti-doped and V-doped Mg nanorod arrays in a high vacuum physical vapor deposition system. These nanostructures have shown better hydrogen sorption kinetics compared to those fabricated by the ball-milling technique [23–26].

For H_2 storage in metal hydrides, the hydrogenation and dehydrogenation processes are always accompanied by heat generation and release. During the hydrogenation process, the hydrogen molecules are dissociated, the hydrogen atoms are captured in the interstitial space between metal atoms and heat is generated. During the dehydrogenation process, external heat is needed [27]. Thus, heat has to be removed for the exothermic formation process and added for the endothermic decomposition process. As a result, heat transfer properties of metal hydrides are very important for determining the hydrogen sorption kinetics. In addition, the thermal transport will influence the rate of reaction. Insufficient thermal transport will reduce the hydrogenation and dehydrogenation rate of metal hydrides and, in the worst case, bring the metal hydride formation to a stop [28]. Consequently, the thermal conductivity of metal hydrides is needed for the design of its practical layout. Hahne and Kallweit adopted a transient hot wire method to determine the effective thermal conductivity of a powdery material [1]. The effects of hydrogen pressure, temperature and hydrogen-to-metal concentration on the thermal conductivity for $LaNi_{4.7}Al_{0.3}H_x$ were investigated. Kapischke and Hapke applied a transient technique to characterize the effective thermal conductivity of an MgH_2 bed in a high temperature range of 573–673 K and for a hydrogen pressure atmosphere up to 5 MPa [29]. They also introduced an oscillating heating method to measure the effective thermal conductivity of MgH_2 produced by fine-grained Mg powder in a non-permeated packed cylinder bed reactor in a temperature range of 523–653 K [27]. Recently, many numerical models accompanied by experimental validations were introduced to predict the mechanism of heat transfer in metal hydride beds [30–33]. According to the simulation done by Førde *et al*, the effective thermal conductivity was found to be one of the most important parameters during hydrogen reaction in porous beds [30]. Asakuma *et al* applied a homogenization method to estimate the effective thermal conductivity of a metal hydride bed by considering the microstructure of the reaction bed [34]. So far, most of the investigations on thermal properties are for micro-powder MgH_2. However, the thermal transport properties depend not only on the bulk material properties but also on microstructures, especially nanostructures. Nanostructure can significantly change the thermal transport property of the same material, thus it could greatly influence the hydrogen sorption dynamics of metal hydrides. Nevertheless, so far, there have been almost no studies on how the thermal transport properties of nanostructured metal hydrides, especially nanostructured MgH_2, are affected by their specific structure and composition. This is mainly due to the lack of a systematic fabrication technique to create metal hydride nanostructures.

In this paper, a unique glancing angle co-deposition technique is used to fabricate V-doped Mg nanorod arrays [35]. The samples are hydrogenated and dehydrogenated for 21 cycles. We apply a photothermal technique and a multilayer physical model [36] to characterize the effective thermal conductivity and density of V-doped Mg hydride nanostructures. The density of the V-doped Mg hydrides is also evaluated by electron micrograph observation, and the two measurement results are compared. The thermal conductivity of bulk V-doped Mg hydrides is also derived based on the measured values.

2. Experimental details

2.1. Sample preparation

The V-doped Mg nanostructures are fabricated using a unique, custom-designed electron-beam evaporation system (Pascal Technology) equipped with a glove box to prevent the sample from exposure to air during the post-fabrication handling. Details of the experimental set-up are described elsewhere [35]. The chamber is evacuated to a base pressure of 10^{-8} Torr. Layers of 1 μm thick Ti film (vapor incident angle $\alpha = 10^\circ$ with respect to the substrate normal) and 0.5 μm thick Ti nanorods ($\alpha = 70^\circ$) are evaporated subsequently onto an Si substrate at a deposition rate of 0.1 nm s^{-1}. Both the Ti film and Ti nanorod arrays are used as a diffusion barrier to prevent Mg alloying with Si. The V dopant is used to catalyze the formation and decomposition of MgH_2 during hydrogen absorption/desorption cycling [37]. The V-doped Mg nanostructures are then deposited on the nanostructured Ti-barrier-coated Si substrate by a co-evaporation of both Mg (0.5 nm s^{-1}) and V ($\sim$0.015 nm s^{-1}) at $\alpha = 70^\circ$ until the quartz crystal microbalance (QCMs positioned to receive the near-normal deposited atoms) reads 20 μm for Mg and 600 nm for V, resulting in a $\sim$4.6 at.% V-doped Mg nanostructure array. The porous structure is expected to enhance the hydrogen sorption kinetics due to its large surface area. The as-deposited samples are cut into 0.5 inch $\times$ 0.5 inch pieces and installed in a PCT Sievert-type apparatus (Hy-energy: PCTPro-2000) for H-absorption (under 10 bar H pressure) and desorption (under vacuum) measurement. After 21 cycles of hydrogenation and dehydrogenation, the hydrogenated samples are taken out for morphological and thermal conductivity characterization.

The morphology of the V-doped Mg nanostructures before and after hydrogenation are characterized by a field emission scanning electron microscope (SEM, FEI Inspect F) and the representative SEM images are shown in figure 1. From the top-view (figure 1(a)) and cross-sectional view (figure 1(b))

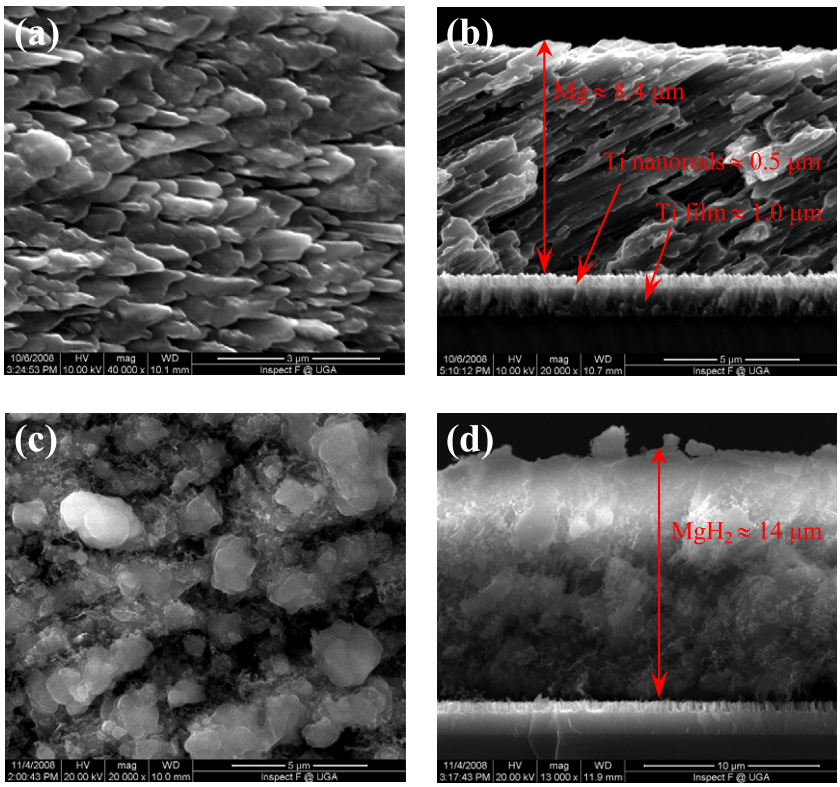

Figure 1. Top-view (a) and cross-sectional (b) SEM images of the as-deposited 4.6% V-doped Mg nanorod sample; top-view (c) and cross-sectional (d) SEM images of the hydrogenated V-doped Mg in the 21st cycle.

SEM images, the as-deposited V-doped Mg sample shows an aligned and tilted nanorod-like array structure with an average height of ∼8.4 μm and rod diameter of ∼300 nm. This array structure is tilting away from the substrate normal at an angle of $\beta \approx 60^\circ$ due to a shadowing effect, similar to the Ti-doped Mg case [23]. In addition, a Ti diffusion barrier layer, consisting of a 0.5 μm Ti nanorod array and a 1 μm Ti film, is visible between the Mg layer and Si substrate, which appears to remain almost unchanged after 21 cycles of H-absorption/desorption (figures 1(b) and (d)), indicating that such a unique structure of a Ti nanorod array on a Ti film can work quite well as the diffusion barrier between Mg and Si [37]. However, a significant morphology change occurs to the hydrogenated V-doped Mg: the original rod structure is totally distorted to form aggregates of sphere-like particles, as shown by the SEM images in figures 1(c) and (d), and the sample height increases to ∼14 μm, corresponding to a height or volume expansion of 67%.

2.2. Experimental details for thermal conductivity measurement

A non-contact photothermal technique is used to measure the thermal conductivity of the hydrogenated V-doped Mg nanostructures on Ti-coated Si substrates. Note that, after hydrogenation, the metals Mg, V and Ti become their hydrides MgH_2, $VH_{0.81}$ and TiH_2 according to x-ray diffraction (XRD) as shown in figure 2 [26]. The principles of the experiment are shown in figure 3(a). The samples are first sputtering-coated with a 200 nm thick Au film on top of the MgH_2 layer. A modulated laser is used to irradiate the surface of the Au film. As the Au film absorbs the laser, the temperature of the Au layer goes up due to laser heating, which will also be affected by the thermal conductivity of the MgH_2 underlayer. Thus, when the periodically modulated laser light gets absorbed by the Au layer, a periodic temperature variation at the Au surface will occur. However, due to the thermal transport in the underlayer, this temperature variation will have a phase shift with respect to the original modulated laser. Therefore, by measuring the phase shift between the thermal radiation from the Au surface and the original laser beam, one can determine the thermophysical properties of the MgH_2 layer. Au is chosen for the surface coating due to its high thermal conductivity and the availability of metal selection in our sputtering coating system (Denton: Desk V).

The schematic of the photothermal experimental set-up is shown in figure 3(b) and the details can be found in our previous work [36, 38]. An infrared diode laser (B & W TEK: BWF-2, 809 nm wavelength) modulated by a function generator is used as the heating source. The output laser power is set to be 219 mW, which will induce a sufficient thermal radiation signal from the sample surface and meanwhile keep the surface temperature low enough to not damage the sample. After the laser beam is reflected and focused, it is directed to the sample surface, which is angled at approximately 45° relative to the incoming laser beam. The laser beam follows the Gaussian distribution and the heating spot size of the laser on the sample surface is approximately 0.7 mm × 1.4 mm [38]. As

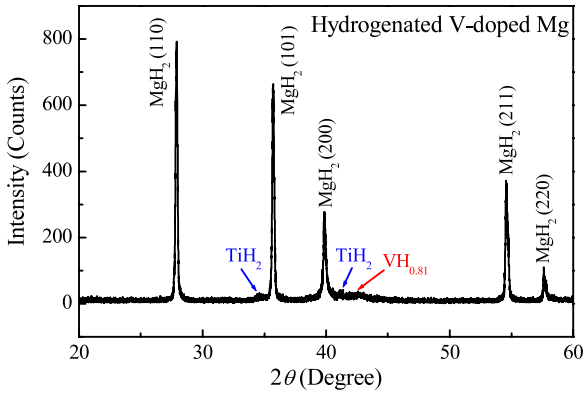

Figure 2. XRD pattern of the hydrogenated (in the 21st cycle) V-doped Mg nanostructures. It shows that, after hydrogenation, the metal Mg (host), V (dopant) and Ti (barrier layer) become their hydrides MgH_2, $VH_{0.81}$ and TiH_2.

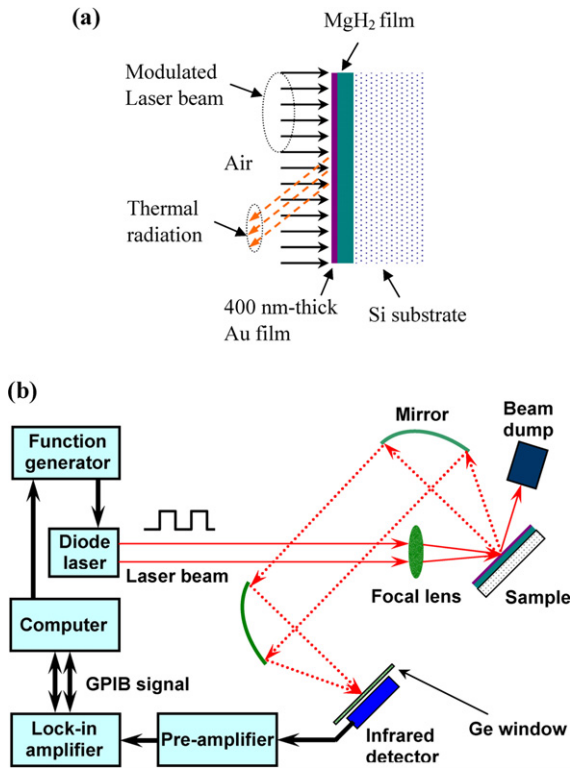

Figure 3. (a) Principle of the photothermal experiment; (b) schematic of photothermal experimental set-up.

the heating spot size is much larger than the thermal diffusion depth in the lateral direction of the sample, we can take the beam as a uniformly distributed incident beam. Thus, the thermal conduction in the Au and MgH_2 layers can be treated as one dimensional (1D). The specular reflection of the laser beam from the Au film is collected by a beam dump. The thermal emission from the Au film is collected by two off-axis paraboloidal mirrors and is directed into an infrared detector (Judson Technology: J15D12). A Ge window, which only allows the thermal emission to pass through, is placed in front of the detector to filter the diffuse reflection. The signal

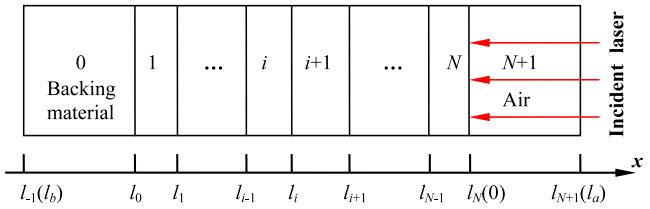

Figure 4. Schematic of N-layer model [39].

from the infrared detector is transferred to a pre-amplifier and measured by a lock-in amplifier (Stanford Research: SR830) which is controlled by a PC for data acquisition.

For a multilayer 1D diffusion problem as shown in figure 4, the thermal diffusion equation in layer i can be expressed as [39]

$$\frac{\partial^2\theta_i}{\partial x^2} = \frac{1}{\alpha_i}\frac{\partial\theta_i}{\partial t} - \frac{\beta_i I_0}{2k_i}\exp\left(\sum_{m=i+1}^{N} -\beta_m L_m\right)\times e^{\beta_i(x-l_i)}(1+e^{j\omega t}), \quad (1)$$

where $\theta_i = T_i - T_{amb}$ and $L_i = l_i - l_{i-1}$ are the modified temperature and thickness of layer i, respectively, and T_{amb} is the ambient temperature. α_i, β_i and k_i are the thermal diffusivity, optical absorption and thermal conductivity of layer i, respectively. The solution θ_i to the equation consists of three parts: the transient component $\theta_{i,t}$, the steady DC component $\bar{\theta}_{i,s}$ and the steady AC component $\tilde{\theta}_{i,s}$. Only the AC component $\tilde{\theta}_{i,s}$ needs to be evaluated and can be picked up by the lock-in amplifier. Details of the photothermal principles and solution can be found in [36, 38, 39].

3. Results and discussion

3.1. System calibration

The phase shift between the thermal radiation and the modulated laser is the parameter we want to measure for calculating the thermophysical properties of the samples. The experimental system, however, will inevitably have a systematic phase shift during the operation. This phase shift can be determined by measuring the phase shift (calibration data) between the reflected laser beam from the sample and the original laser beam. If the experimental set-up is perfect, the phase shift should be zero. This system phase shift is ruled out by subtracting the calibration phase shift from the measured phase shift at the corresponding frequencies [36, 39] in real measurement. Figure 5 shows the measured phase shift of the reflected laser beam at the modulation frequency range from 17 to 400 Hz. The calibration phase shift induced by the experimental system can be calculated in the form of a time lag as $\phi_{cal}/360/f$, where ϕ_{cal} and f are the calibration phase shift and modulation frequency, respectively. The phase shift as well as the time lag of the experimental set-up is shown in figure 5. The system time lag is 1.5–190 μs, which could be induced by the irregularity of the wave shape from the function generator.

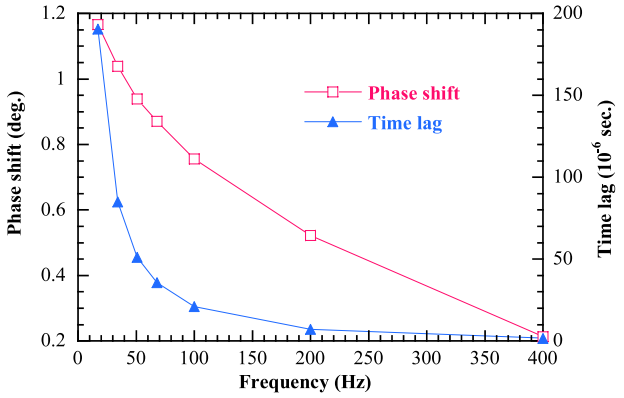

Figure 5. The calibrated phase shift ϕ_{cal} of reflected laser beam and time lag of the photothermal measurement system.

3.2. Measurement results for MgH_2

The Au layer is used to absorb the laser power and generate the temperature gradient that can propagate into the V-doped Mg hydrides and emit thermal radiation for detection. The optical absorption length of Au for the laser with the wavelength $\lambda = 809$ nm is 13.2 nm [40]. Considering the roughness of the V-doped Mg hydride sample surface shown in figures 1(c) and (d), we coat a 200 nm thick Au film on the top surface instead of a thinner layer. In order to make sure the coating is thick enough to absorb the laser beam completely and avoid the laser going through the Au layer, after the measurements with the 200 nm Au coating, another 200 nm thick Au film is coated on the sample and the thermal radiation is measured again. These two measurements are compared to verify that the infrared laser is completely absorbed by the Au film.

After the experimental set-up is calibrated, the phase shift of the thermal radiation is measured in a low frequency range of 17–400 Hz. The reason we choose a low frequency range is that, under a high frequency, the thermal diffusion depth would not exceed the roughness size of the sample. This will impose greater difficulty on data analysis. The phase shift ϕ_t between the thermal radiation and the modulated laser beam is the difference of the measured phase shift of thermal radiation ϕ_{mea} and the calibrated phase shift ϕ_{cal} at the corresponding frequencies, $\phi_t = \phi_{mea} - \phi_{cal}$. The filled symbols in figure 6 show the typical phase shift ϕ_t at different laser modulation frequencies f for 200 nm and 400 nm Au coatings, respectively. For both cases, the ϕ_t–f relationship follows the same trend: ϕ_t increases rapidly when f changes from 17 to 100 Hz modulation frequency, it reaches a maximum at $f = 200$ Hz and then slowly decreases at higher frequencies. These results can be fitted by a multilayer heat transfer model developed by Hu *et al* [39]. In our experiments, the multilayer model includes four layers, the air at the top of the Au film, the Au film, the V-doped Mg hydrides layer and the Si substrate. We take the TiH_2 layer of a 1 μm thick film and 0.5 μm thick nanorod array as part of the MgH_2 layer (the reason for neglecting the thermal transport effect of this layer will be discussed later). With a knowledge of the properties of air, Au, Si substrate, as well as the thickness of an equivalent MgH_2 layer, 15.5 μm, different values for thermal conductivity and

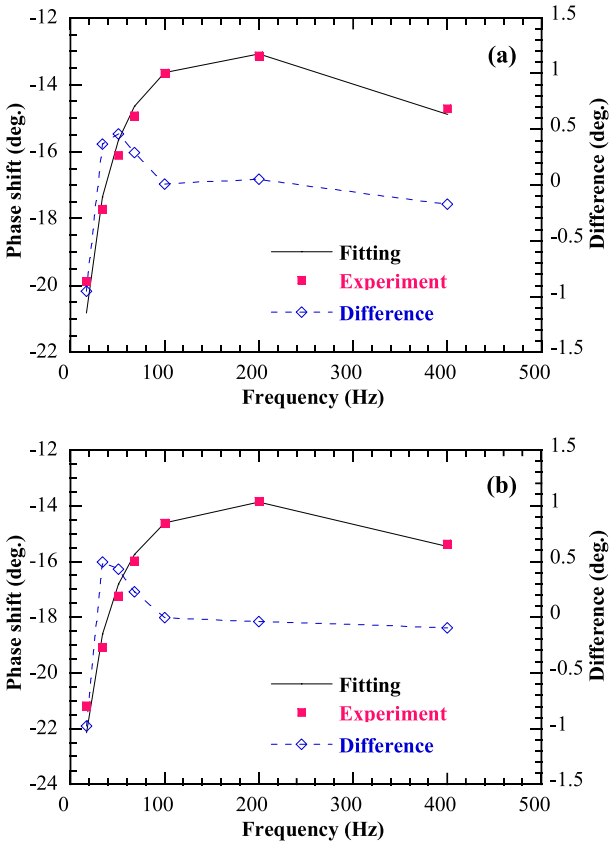

Figure 6. The phase shift ϕ_t of the thermal radiation from the MgH_2 surface of sample #1 with 200 nm (a) and 400 nm (b) thick Au film versus different modulation frequencies f.

density of the hydrogenated V-doped Mg nanostructures in the model are tried to obtain the best fitting. The values tried, giving the best fit to the experimental data, are taken as the values of the properties.

The solid curves in figure 6 show the best fittings for sample #1 with 200 and 400 nm Au coatings, respectively. For the 200 nm Au coated sample, the obtained effective thermal conductivity k_{eff} is 1.94 W m^{-1} K^{-1} and the density ρ of V-doped MgH_2 is 916 kg m^{-3}. For the 400 nm Au coated sample, $k_{eff} = 2.17$ W m^{-1} K^{-1} and $\rho = 940$ kg m^{-3}. For both cases, the fitting results agree with the experimental data quite well: the difference between the fitting and the experimental data fluctuates in the range of $\pm 0.5°$, while the largest difference is only $-1°$, which is an acceptable uncertainty in the experiment.

The measured effective thermal conductivity k_{eff} and density ρ of three different pieces of V-doped Mg hydride samples are summarized in table 1. For the sample with 200 and 400 nm thick Au coatings, the obtained k_{eff} and ρ values always agree well with each other. Thus, it is safe to conclude that the 200 nm Au coating is thick enough to absorb the incident laser beam and prevent the laser from going through the Au layer. For different samples, ρ varies from 878 to 1031 kg m^{-3}, which are smaller than the bulk density of MgH_2, 1450 kg m^{-3} [27]. This low density is caused by the porosity of the sample. The measured k_{eff} varies in the range of 1.60–2.17 W m^{-1} K^{-1}. The large variations in both ρ and k_{eff}

Table 1. Measurement results of different samples.

Sample #	1		2		3	
Au thickness (nm)	200	400	200	400	200	400
ρ (kg m^{-3})	916	940	878	952	1018	1031
k_{eff} (W m^{-1} K^{-1})	1.94	2.17	2.00	2.12	1.60	2.02
φ (%)	36.8	35.2	39.4	34.3	29.8	28.9
k_{bulk} (W m^{-1} K^{-1})	3.63	3.94	3.95	3.78	2.62	3.25

Table 2. Measurement results at five different spots of sample #3 with 400 nm thick gold film.

Measurement point	1	2	3	4	5
ρ (kg m^{-3})	1031	1216	917	1212	1320
k_{eff} (W m^{-1} K^{-1})	2.02	1.50	1.16	2.40	2.00
φ (%)	28.9	16.1	36.8	16.4	9.0
k_{bulk} (W m^{-1} K^{-1})	3.25	1.93	2.17	3.11	2.30

from sample to sample could be caused by the nonuniformity of the V-doped Mg hydride nanostructured sample, as shown in figures 1(c) and (d). To confirm this hypothesis, we have performed five measurements on different locations of sample #3 with a 400 nm Au coating. These five points are located at the center and the four corners of the sample, and the obtained k_{eff} and ρ are summarized in table 2. Clearly both k_{eff} and ρ depend strongly on the locations: k_{eff} varies from 1.16 to 2.40 W m^{-1} K^{-1} and ρ changes from 917 to 1320 kg m^{-3}. Those variations are comparable to the sample-to-sample variations and they may come from three factors: the measurement uncertainty, the nonuniform morphology of the V-doped Mg hydride sample and the different thicknesses at different spots. The porosity will strongly affect the measurement results, as will be discussed later. A close look at figures 1(c) and (d) reveals that the hydrogenated V-doped Mg is not uniform across the entire thickness. One can discern from figure 1(d) that the shade of color of the cross-sectional view SEM image varies from place to place, indicating that the porosity or density of the materials is not homogeneous. Both the top-view and cross-sectional view SEM images shown in figures 1(c) and (d) demonstrate that the surface of the hydrogenated sample consists of micro-sized grains that are not uniformly distributed, which causes the thickness variation.

The measured effective thermal conductivity k_{eff} is in the range of 1.16–2.40 W m^{-1} K^{-1}, which is considerably different from those reported in the literature. Stapßburger [41] found the temporal and local average effective thermal conductivity of MgH_2 to be 7.0–9.5 W m^{-1} K^{-1} for the dehydrogenation process at T = 543–643 K. Kallweit [42] used a transient technique and obtained k_{eff} = 6–7 W m^{-1} K^{-1} for T = 553 K and k_{eff} = 7–8 W m^{-1} K^{-1} for T = 593 for MgH_2 under isothermal conditions. Kapischke and Hapke [29] applied a transient measurement method and obtained an effective thermal conductivity of 3–9 W m^{-1} K^{-1} for the dehydrogenation process in an MgH_2 bed at T = 573–673 K and H_2 pressure up to 5 MPa. They also used an oscillating heating method to obtain the effective thermal conductivity of fine-grained MgH_2 in a non-permeated packed bed under different hydrogen-to-metal ratios during the hydrogenation process in the temperature range of 523–653 K [27]. They found that k_{eff} = 2–8 W m^{-1} K^{-1}, and close to the completion of hydrogenation, k_{eff} = 1.8–2.4 W m^{-1} K^{-1}. In our experiment, the V-doped Mg samples are fully hydrogenated before the thermal transport measurement on the one hand; on the other hand, our thermal measurement temperature is 298 K, which is lower than those by Kapischke and Hapke. Considering the fact that, at low temperature, due to the decreasing conductivity of the solid particle grid [43] or on the other hand, the increasing electrical resistivity [44], the effective thermal conductivity decreases slightly when temperature increases, our measurements qualitatively agree with the measurements in [27]. Other measurement results are mostly obtained during the hydrogenation process. Due to partial hydrogenation, the remaining Mg clusters in the structure will play a significant role in determination of the effective thermal conductivity. Thus, it is understandable that the k_{eff} measured during the hydrogenation process is much larger than those we measured. Furthermore, the nanostructures in our samples will also reduce the thermal conductivity due to increased phonon scattering.

3.3. The effect of porosity on thermal conductivity

The effective thermal conductivity reported above is affected by many factors, such as the porosity, the microstructure and the small amount of V hydride in the MgH_2. Among them, the porosity plays a critical role. The effective thermal conductivity k_{eff} of a porous material is determined by the porosity φ (the volume porosity factor) and bulk thermal conductivity k_{bulk} through Maxwell's correlation [45]:

$$\frac{k_{\text{eff}}}{k_{\text{bulk}}} = 1 + \frac{3(\gamma - 1)\varphi}{(\gamma + 2) - (\gamma - 1)\varphi}, \tag{2}$$

where γ is the ratio of thermal conductivity of the pore material (air) to that of the nanostructure material (MgH_2). Since the thermal conductivity of air, 0.026 W m^{-1} K^{-1}, is significantly smaller than that of MgH_2 (see the above discussions), we can assume that $\gamma = 0$. The porosity φ can be calculated as

$$\varphi = 1 - \frac{(\rho c_p)_{\text{eff}}}{(\rho c_p)_{\text{bulk}}}, \tag{3}$$

where $(\rho c_p)_{\text{eff}}$ and $(\rho c_p)_{\text{bulk}}$ are the measured effective volumetric specific heat and bulk volumetric specific heat, respectively. For a composite system with n types of materials, $(\rho c_p)_{\text{bulk}}$ can be computed as

$$(\rho c_p)_{\text{bulk}} = \sum_{i}^{n} \varphi_i \rho_i c_{p,i}, \tag{4}$$

where φ_i is the volume fraction of component i. In equation (4), the hydrogenated V-doped Mg sample can be treated as a composite of MgH_2, $VH_{0.81}$ and TiH_2. Since the layers of the TiH_2 film and nanorod array do not mix with the doped MgH_2, and their thicknesses (1.5 μm) are much smaller than that of the doped MgH_2 layer (14 μm), we can neglect the effects of the TiH_2 layers. It is known that the atomic fractions of the Mg and V elements in the sample are

95.4% and 4.6%. After hydrogenation, the atomic fractions of MgH_2 and $VH_{0.81}$ are also 95.4% and 4.6%. Consequently, we can also neglect the effect of $VH_{0.81}$, which means we take the composite film as pure MgH_2 for first-order estimation to estimate the bulk ρc_p. Such an approximation will introduce very little uncertainty due to the low concentration of $VH_{0.81}$. The bulk density and specific heat of MgH_2 are 1450 kg m^{-3} and 1440 J kg^{-1} K^{-1}, respectively, and the volumetric specific heat $(\rho c_p)_{\text{bulk}}$ of the hydrogenated V-doped Mg nanostructures calculated according to equation (4) is 2088 kJ m^{-3} K^{-1} at 298 K. The effective volumetric specific heat $(\rho c_p)_{\text{eff}}$ of the hydrogenated V-doped Mg nanostructures is calculated based on the measured density ρ and specific heat (here we use 1440 J kg^{-1} K^{-1}). The values are in the range of 1264–1901 kJ m^{-3} K^{-1}, which is smaller than that of bulk composite MgH_2 and $VH_{0.81}$. According to equation (3), the porosity φ of the composite film is predicted to be in the range of 9.0–39.4%, which indicates that the porosity varies a lot from sample to sample. Even at different spots on the same sample, the porosity changes dramatically. This nonuniformity could mainly come from the sample hydrogenation/dehydrogenation cycling process. The deposition could not be perfect to form an evenly distributed crystal array of Mg and V. What is more is that the hydrogenation process could not be uniform, either. The extent of hydrogenation would also affect the distribution of cavities. With the knowledge of volume porosity factors and the effective thermal conductivity, the thermal conductivity of bulk composite films without porosity is derived and listed in the last rows of tables 1 and 2. The bulk thermal conductivity varies from 1.96 to 3.99 W m^{-1} K^{-1}. Such large variation could result from the structure of the MgH_2 itself.

In order to estimate the effect of the TiH_2 layer, the thermal resistance of the TiH_2 layer is compared with that of the layer of the V-doped Mg hydrides. For the TiH_2 film layer, its thermal resistance is l_1/k, where l_1 is the thickness of the film and k is the bulk thermal conductivity. Since there is no data available for the thermal conductivity of TiH_2 at room temperature, we use the thermal conductivity of $TiH_{1.97}$ instead, 28.4 W m^{-1} K^{-1} [46]. For the TiH_2 nanorod layer, we just take the bulk thermal conductivity multiplied by a coefficient as the thermal conductivity of the nanorods, i.e. βk (β = 0.1–0.5 is for the volumetric concentration of the nanorods). The thermal resistance of the TiH_2 nanorod layer is $l_2/(\beta k)$, where l_2 is the length along the axial direction of the nanorods. Consequently, the thermal resistance of the TiH_2 layer is 7.0–21.1 $\times$ 10^{-8} K m^2 W^{-1}, while the thermal resistance of the layer of V-doped Mg hydrides is 6.46–13.4 $\times$ 10^{-6} K m^2 W^{-1}, which is approximately two orders of magnitude larger than that of the TiH_2 layer. Therefore, the TiH_2 layer has a negligible effect on the final fitting results. Another thing we must bear in mind is the radiation between the TiH_2 nanorods, which will obviously strengthen heat transfer, thereby decreasing the thermal resistance of the TiH_2 layer. This will make our above conclusion safer.

For the thermal conductivity reported in this work, it is affected by several factors: (1) increased phonon scattering by the nanostructures, (2) volume fraction of the pores inside (porosity level), (3) pore size, pore-to-pore separation and pore shape, and (4) surface roughness. During data processing, we focused on the effect of the volume fraction (porosity level). Therefore the k_{bulk} calculated in tables 1 and 2 still has the effect of phonon scattering at the nanograin boundary, the effect of the pore characteristics (size, shape and separation), as well as surface roughness and structure nonuniformity. These effects cannot be ruled out since no data is available about them. There is no conclusive trend for the correlation between the porosity and k_{eff} based on the data reported in tables 1 and 2. This is because, for each point/sample we measured in the work, they could have different pore size, shape and separation, even if we can characterize their porosity level. Therefore, the varying pore characteristics (structure nonuniformity) make the trend inconclusive. On the other hand, since we can characterize the porosity level, we can clearly rule out this effect.

3.4. Comparison of measured density and porosity with electron micrograph observation

In SEM observation, the porosity φ is estimated according to $\varphi = 1 - m/\rho/V$, where V is the volume of the sample as $V = Ah$, A is the projected substrate area, and h is the sample height, which is estimated to be 8.4 μm (for Mg) and 14 μm (for MgH_2) using SEM observations, as shown in figures 1(b) and (d). m and ρ are respectively the mass and bulk density of Mg in the as-deposited sample or the mass and bulk density of MgH_2 in the hydrogenated sample. According to the sample fabrication process, the total mass of Mg on 78 pieces of 0.5 inch $\times$ 0.5 inch substrates is $m_{\text{Mg}} \approx$ 137 mg, measured by an electronic balance. After 21 cycles of hydrogenation/dehydrogenation, a complete hydrogenation state is reached, which has been verified by neutron scattering experiments. The total mass of MgH_2 can be estimated while ignoring the dopant V, $m_{\text{MgH}_2} = m_{\text{Mg}} \times (M_{\text{Mg}} + 2M_{\text{H}})/M_{\text{Mg}} \approx$ 148 mg, where M_{Mg} and M_{H} are the atomic weights of Mg and H elements, respectively. Thus, the density of the sample is derived as $\rho_{\text{sample}} = m_{\text{MgH}_2}/V_{\text{sample}} \approx$ 841 kg m^{-3}, which is close to those measured by the photothermal experiments: 878–1320 kg m^{-3}. Therefore, the density estimation based on the SEM observation provides a good reference and validates the measurements by the photothermal experiments. For the bulk material, $\rho_{\text{Mg}} = 1740$ kg m^{-3} and $\rho_{\text{MgH}_2} = 1450$ kg m^{-3}. Consequently, the porosity can be estimated to be $\varphi \approx$ 25% for the as-deposited sample and $\varphi \approx$ 42% for the hydrogenated sample. The porosity φ (for MgH_2) calculated from photothermal experiments is 9.0–39.4%, whose upper limit is close to the SEM observation.

4. Conclusion

In this work, the thermal conductivity and density of hydrogenated V-doped Mg nanostructures were investigated using the photothermal technique. In addition, the thermal conductivity of bulk MgH_2 was also evaluated based on the measured effective values. Our experimental results showed that the effective thermal conductivity of the V-doped Mg hydride nanostructures was in the range of 1.16–2.40 W m^{-1} K^{-1}, the bulk thermal conductivity was in the

range of 1.93–3.95 W m^{-1} K^{-1} and the density falls in the range of 878–1320 kg m^{-3}. The density results by the photothermal measurement agree well with those estimated from SEM analysis. Because of the surface roughness and nonuniformity of the nanostructures, the effective thermal conductivity and density vary at different testing points and different samples.

Acknowledgments

Support of this work by the start-up fund from Iowa State University and NSF (CBET-0931290) is gratefully acknowledged. The authors also thank the great help from Ms Liying Guo during the initial characterization. YPH and YPZ were supported by the DOE Hydrogen Initiative Award (DE-FG02-05ER46251). The authors would like to thank Wilson Smith for proofreading the manuscript.

References

[1] Hahne E and Kallweit J 1998 *Int. J. Hydrog. Energy* **23** 107–14
[2] Trudeau M L 1999 *MRS Bull* **24** 23–6
[3] Sakintuna B, Lamari-Darkrim F and Hirscher M 2007 *Int. J. Hydrog. Energy* **32** 1121–40
[4] Kelkar T, Kanhere D G and Pal S 2008 *Comput. Mater. Sci.* **42** 510–6
[5] Kelekar R, Giffard H, Kelly S T and Clemens B M 2007 *J. Appl. Phys.* **101** 114311
[6] Pozzo M and Alfe D 2009 *Int. J. Hydrog. Energy* **34** 1922–30
[7] Huot J, Liang G, Boily S, Van Neste A and Schulz R 1999 *J. Alloys Compounds* **293–295** 495–500
[8] Zaluska A, Zaluski L and Ström-Olsen J 2001 *Appl. Phys.* A **72** 157–65
[9] Shang C X, Bououdina M, Song Y and Guo Z X 2004 *Int. J. Hydrog. Energy* **29** 73–80
[10] Song Y, Guo Z X and Yang R 2004 *Phys. Rev.* B **69** 094205
[11] Song Y, Zhang W C and Yang R 2009 *Int. J. Hydrog. Energy* **34** 1389–98
[12] Tsuda M, Diño W A, Kasai H, Nakanishi H and Aikawa H 2006 *Thin Solid Films* **509** 157–9
[13] Liang G 2004 *J. Alloys Compounds* **370** 123–8
[14] Liang G, Huot J, Boily S, Van Neste A and Schulz R 1999 *J. Alloys Compounds* **292** 247–52
[15] Schulz R, Liang G and Huot J 2001 *Proc. 22nd Risø Int. Symp. on Material Science: Science of Metastable and Nanocrystalline Alloys: Structure, Properties and Modeling* ed A R Dinesen (Roskilde: Risø National Laboratory) pp 141–53
[16] Bobet J L, Aymonier C, Mesguich D, Cansell F, Asano K and Akiba E 2007 *J. Alloys Compounds* **429** 250–4
[17] Schmidt H, Jonschker G, Goedicke S and Mennig M 2000 *J. Sol–Gel Sci. Technol.* **19** 39–51
[18] Léon A, Knystautas E J, Huot J, Lo Russo S, Koch C H and Schulz R 2003 *J. Alloys Compounds* **356** 530–5
[19] Gedanken A 2007 *Ultrason. Sonochem.* **14** 418–30
[20] Zhitomirsky I 2006 *J. Mater. Sci.* **41** 8186–95
[21] Wang Y, Sasaki M, Goto T and Hirai T 1990 *J. Mater. Sci.* **25** 4607–13
[22] Armelao L, Barreca D, Bottaro G, Gasparotto A, Gross S, Maragno C and Tondello E 2006 *Coord. Chem. Rev.* **250** 1294–314
[23] He Y, Zhao Y and Wu J 2008 *Appl. Phys. Lett.* **92** 063107
[24] He Y, Zhao Y, Huang L, Wang H and Composto R J 2008 *Appl. Phys. Lett.* **93** 163114
[25] He Y and Zhao Y 2009 *Phys. Chem. Chem. Phys.* **11** 255–8
[26] He Y and Zhao Y 2009 *Nanotechnology* **20** 204008
[27] Kapischke J and Hapke J 1998 *Exp. Therm. Fluid Sci.* **17** 347–55
[28] Groll M 1993 *J. Heat Recovery Syst. CHP* **13** 341–6
[29] Kapischke J and Hapke J 1994 *Exp. Therm. Fluid Sci.* **9** 337–44
[30] Førde T, Nœss E and Yartys V A 2009 *Int. J. Hydrog. Energy* **34** 5121–30
[31] Griesinger A, Spindler K and Hahne E 1999 *Int. J. Heat Mass Transfer* **42** 4363–74
[32] Sun D W and Deng S J 1990 *Int. J. Hydrog. Energy* **15** 331–6
[33] Nakagawa T, Inomata A, Aoki H and Miura T 2000 *Int. J. Hydrog. Energy* **25** 339–50
[34] Asakuma Y, Miyauchi S, Yamamoto T, Aoki H and Miura T 2004 *Int. J. Hydrog. Energy* **29** 209–16
[35] He Y, Zhang Z, Hoffmann C and Zhao Y 2008 *Adv. Funct. Mater.* **18** 1676–84
[36] Wang T, Wang X, Zhang Y, Liu L, Xu L, Liu Y, Zhang L, Luo Z and Cen K 2008 *J. Appl. Phys.* **104** 013528
[37] He Y and Zhao Y 2009 *J. Alloys Compounds* **482** 173–86
[38] Wang X, Zhong Z and Xu J 2005 *J. Appl. Phys.* **97** 064302
[39] Hu H, Wang X and Xu X 1999 *J. Appl. Phys.* **86** 3953–8
[40] Weaver J H and Frederikse H P R 2007 *CRC Handbook of Chemistry and Physics, Internet Version 2007, (Edi 87)* ed D R Lide (Boca Raton, FL: CRC Press, Taylor and Francis) pp 12–120
[41] Stapßburger K 1992 *PhD Thesis* University of Essen, Germany
[42] Kallweit J 1994 *PhD Thesis* University of Stuttgart, Germany
[43] Suissa E, Jacob I and Hadari Z 1984 *J. Less-Common Met.* **104** 287–95
[44] Klemens P 1969 *Thermal Conductivity* vol 1, ed R P Tye (London: Academic) p 173
[45] Maxwell J C 1873 *Electricity and Magnetism* (Oxford: Clarendon)
[46] Tsuchiya B, Nagata S, Shikama T, Konashi K and Yamawaki M 2003 *J. Alloys Compounds* **356/357** 223–6